An integrated 3C-silicon carbide-on-insulator photonic platform for nonlinear and quantum light sources

Check for updates

Jiayang Li [ID], Qianni Zhang [ID], Jiantao Wang [ID] & Andrew W. Poon [ID] ✉

Silicon carbide (SiC) polytypes are emerging for integrated nonlinear and quantum photonics due to their wide-bandgap energies, second-order optic nonlinearity and process compatibility with complementary metal-oxide-semiconductor technologies. Among polytypes, 3C-SiC is the only one epitaxially grown on wafer-scale silicon substrates. However, on-chip nonlinear and quantum light sources leveraging the second-order nonlinearity of 3C-SiC have not been reported to our knowledge. Here, we design and fabricate an elliptical microring on 3C-SiC. We demonstrate a nonlinear light source with a second-harmonic generation efficiency of $17.4 \pm 0.2\% \, W^{-1}$ and difference-frequency generation with a signal-idler bandwidth of 97 nm. We demonstrate a spontaneous parametric down-conversion source with a photon-pair generation rate of 4.8 MHz and a coincidence-to-accidental ratio of 3361 ± 84. We measure a low heralded single-photon second-order coherence $g_H^{(2)} = 0.0007$. We observe time-bin entanglement with a visibility of $86.0 \pm 2.4\%$ using this source. Our work paves a way toward SiC-based on-chip nonlinear and quantum photonic circuits.

The silicon carbide (SiC) semiconductor industry is expanding rapidly driven by the growing needs for high-power electronics[1]. Meanwhile, integrated photonic platforms based on SiC polytypes are emerging in recent years, including hexagonal (4H-, 6H-) SiC and cubic (3C-) SiC. They offer a wide bandgap energy from 2.3 to 3.2 eV[2], which enables transmissions of visible light and does not suffer from nonlinear two-photon absorption at the 1550/1310 nm telecommunications wavelengths. They also feature a high hardness for photon-phonon interactions[3], a fast heat dissipation for high-speed directly modulated lasers[4] and different color centers for single quantum emitters[5,6]. Owing to their non-centrosymmetric crystal lattices, SiC polytypes feature second-order nonlinear susceptibilities $\chi^{(2)}$. For example, 3C-SiC features $\chi^{(2)}_{zxy} \approx 34 \, \text{pm V}^{-1}$ (theoretical)[7] while 4H-SiC features $\chi^{(2)}_{zzz} \approx -23.4 \, \text{pm V}^{-1}$ and $\chi^{(2)}_{zxx} \approx 13.0 \, \text{pm V}^{-1}$ [8] This enables nonlinear and spontaneous quantum light sources based on $\chi^{(2)}$ optic processes on integrated SiC-on-insulator (SiCoI) platforms. Compared with the integrated lithium niobate-on-insulator (LNoI) platform, SiC offers process compatibility with the mature wafer-level complementary metal-oxide-semiconductor compatibility (CMOS) processes and an insignificant photorefractive effect[9–11]. Supplementary Table 1 (see Supplementary Note 1) summarizes and compares conventional integrated second-order nonlinear photonic platforms.

Nonetheless, none of the crystalline SiC polytypes offers a large refractive index contrast with their native substrates. Photonic devices on SiC are thus often fabricated on suspended SiC films[12–15] and on the SiCoI platforms[11,16–21]. Integrated SiCoI platforms rely on molecular bonding[16–21] or anodic bonding[11] to transfer the SiC films onto SiO_2 substrates, which enables a better scalability for larger-scale integrated photonic circuits. The optical nonlinearity of SiC have been studied last decade[13,15]. Optical parametric oscillation and soliton generation are demonstrated based on high-quality-factor (high-Q) ($>10^6$) microresonators on a 4H-SiCoI platform[17,18] while four-wave mixing is demonstrated on a suspended 3C-SiC platform with relatively lower Q factors (~ 7400)[14]. The demonstration of $\chi^{(2)}$ nonlinearity-based sources remains a challenge partly due to the difficulty to attain the phase-matching condition across an octave while engineering the waveguide dispersion. Recently, second-harmonic generation (SHG) with efficiencies of 360% W^{-1} and 3.91% W^{-1} were demonstrated in 4H-SiCoI using modal phase matching (MPM) and a suspended 4H-SiC microdisk[19,20], respectively. A time-averaged efficiency of 15% W^{-1} using a pulsed laser was demonstrated by using a suspended 6H-SiC photonic-crystal cavity[13]. Moreover, Pockels-effect-based microring modulators have been demonstrated on both 4H- and 3C-SiCoI platforms[21,22]. To our knowledge, spontaneous parametric down

Photonic Device Laboratory, Department of Electronic and Computer Engineering, The Hong Kong University of Science and Technology, Clear Water Bay, Hong Kong, China. ✉e-mail: eeawpoon@ust.hk

conversion (SPDC)-based photon-pair sources have not been demonstrated on SiC platforms.

In this work, we adopted the 3C-SiC as this is the only polytype that is epitaxially grown on wafer-scale silicon substrates. This is promising for future large-scale integration and wafer-scale fabrication. Moreover, an epitaxially grown 3C-SiC layer features a well-controlled thickness, which minimizes the non-uniformity in the SiC film thickness and avoids the material waste during the grinding process which is unavoidable in the case of utilizing a bulk 4H-SiC substrate[20]. We demonstrate on our 3C-SiCoI platform through anodically bonding the 3C-SiC film onto a glass substrate (see Methods). We design a waveguide-coupled elliptical microring resonator using type-I (signal and idler are linearly polarized orthogonally to the pump) MPM for $\chi^{(2)}$-based nonlinear and quantum light sources. We design for the conversion between 780 nm near-visible wavelengths and the 1550 nm near-infrared (NIR) wavelengths. We demonstrate an SHG conversion efficiency of $17.4 \pm 0.2\%$ W^{-1} and difference-frequency generation (DFG) with a non-degenerate signal-idler bandwidth of up to 97 nm. We observe DFG across a bandwidth of 9.5 nm around pumping in the 780 nm wavelengths. We demonstrate a SPDC source with a photon-pair generation rate (PGR) of 4.8 MHz and a coincidence-to-accidental ratio (CAR) of 3361 ± 84 at an on-chip pump power of 5 mW. At this pump power, we obtain a low heralded single-photon second-order coherence $g_H^{(2)} = 0.0007$ with a confidence interval of (0.0001, 0.002) with 68% confidence level using these photon-pairs. We generate a time-bin entanglement with a visibility of $86.0 \pm 2.4\%$ in a free-space Franson interferometer[23] using our photon-pair source, which was reported recently[24]. Our work shows the feasibility of SiC-based on-chip nonlinear and quantum light sources based on $\chi^{(2)}$ nonlinearity.

Results

Nonlinear and quantum light sources using waveguide-coupled elliptical microring cavities

Figure 1a schematically illustrates our elliptical microring resonator as a parametric down-conversion photon-pair source on an integrated 3C-SiCoI platform. We discuss our device design principles starting from classical nonlinearity based on DFG. The zinc-blende unit cell of 3C-SiC features tensor elements $\chi_{zxy}^{(2)} = \chi_{xyz}^{(2)} = \chi_{yzx}^{(2)} \approx 34\,pm\,V^{-1}$,[7]. We adopt this theoretical value because experimental Maker-fringes measurements on bulk 3C-SiC is not available yet[25–27]. These elements mix three waves that are linearly polarized along three orthogonal crystal axes upon satisfying the energy conservation of $\omega_p = \omega_s + \omega_i$, where $\omega_{p,s,i}$ are the angular frequencies of the pump, signal and idler. To minimize the number of waveguide eigenmodes involved in the nonlinear processes, we chose Type-I phase matching noting that 3C-SiC is non-birefringent. As shown in Fig. 1b, based on the (001) 3C-SiC film, we set the NIR input signal and the idler waves around 1550 nm to be transverse electric (TE)-polarized (parallel to the chip) with the x- and y-components of the fields, while the pump wave around 780 nm to be transverse magnetic (TM)-polarized with the z-component of the field. We must satisfy the phase-matching condition of $\beta_p = \beta_s + \beta_i$, where $\beta_{p/s/i}$ are the propagation constants of the three waveguide modes.

A few conventional phase-matching techniques, including periodic-poling-based quasi-phase-matching (QPM)[28,29], birefringence-based phase-matching[30] and cyclic QPM[31], are not available for the 3C-SiC material. We

chose to design for a MPM, where we adopted a higher-order TM_{20} mode at the pump wavelength to match the effective refractive index of the fundamental TE_{00} mode at the signal/idler NIR wavelengths.

We must account for the $\bar{4}3m$ crystal point-group symmetry of 3C-SiC[32] for designing a microring cavity. When the three mixing fields propagate in an arbitrary direction within the (001) 3C-SiC film, the projection of the field of the TE-mode onto the x- and y-crystal axes results in an angle-dependent effective susceptibility $\chi_{eff}^{(2)} = \cos\varphi\,\sin\varphi\,\chi_{zxy}^{(2)}$[33]. The $\chi_{eff}^{(2)}$ is optimized with the waves propagating in directions 45 / 135° between the x- and y-crystal axes. The nonlinear polarization of a $\bar{4}3m$ crystal has a π-phase flip with the wave propagation directions rotated by 90°. While we may leverage this characteristic property to attain $\bar{4}$-QPM, as theoretically studied and experimentally demonstrated in compound III-V material systems featuring the $\bar{4}3m$ crystal symmetry[34–36], this method typically imposes a few-micron cavity size for microdisk resonators which may limit the Q factor[34,35]. The design principle also involves careful alignment of resonances with a certain mode-order difference[34–36]. These impose an overall tight tolerance for device fabrication. Figure 1c schematically illustrates our mitigation of adopting an elliptical cavity. In our scheme, to attain efficiently phase-matched nonlinear processes within microring cavities, we designed an elliptical microring cavity, with a major-to-minor-axes aspect ratio of 2 to increase the MPM interaction length along the flat arc waveguide in one 90° rotation of the fields while decreasing the reverse conversion around the two high-curvature poles. We adopted a semi-major axis $a = 30\mu m$ and a semi-minor axis $b = 15\mu m$, which corresponds to a circumference $L = 145\mu m$, to enable a smaller mode volume compared with mm-sized cavities.

Numerical simulations for attaining MPM

We first fix the pump wavelength at 780 nm and assume degenerate signal and idler wavelengths at 1560 nm. Figure 2a shows the numerically simulated electric-field amplitude distributions of a TE_{00} mode at 1560 nm and a TM_{20} mode at 780 nm, respectively, using a finite-difference eigenmode tool. To search for the potential waveguide geometry to match the effective refractive index of the two modes, we systematically vary the thickness and the width of the rib waveguide structure. Based on our previous device fabrication results, we assumed a symmetric waveguide sidewall slope of 86°. We kept a thin 3C-SiC slab of 100 nm un-etched to avoid undercutting the SiO_2 layer underneath the SiC waveguide. The 3C-SiC is clad by a SiO_2 layer with a thickness of 500 nm. We adopted a Cauchy model with A, B coefficients of 2.553 and 0.0353[9] to calculate the material index of 3C-SiC. To simplify the simulation and design, we assume a straight waveguide structure. Figure 2b shows the numerically simulated effective refractive indices of the two modes with different 3C-SiC film thicknesses as a function of the waveguide width. The width corresponds to the top side of the trapezoidal waveguide cross-section. We can attain the MPM with a waveguide width of 1000 nm and a thickness of 800 nm. The MPM width increases with the 3C-SiC film thickness while the mismatch between the effective refractive indices becomes more tolerant to the waveguide width variation with a thick film.

We designed the waveguide dimensions at a thickness of 800 nm and a top width of 1000 nm, with a slab thickness of 100 nm. Figure 2c shows the numerically simulated non-degenerate DFG effective refractive indices n_{eff} of the modes with wavelengths. Figure 2d shows the numerically simulated

Fig. 1 | Design principles of a 3C-SiC-on-insulator elliptical microring resonator. a Schematics of a parametric down-conversion photon-pair source on a 3C-SiCoI platform. **b** Schematics of the Type-I phase-matching process. **c** Illustration of an elliptical microring cavity with the normalized effective nonlinearity $\chi_{eff}^{(2)}/\chi_{zxy}^{(2)} = \cos\varphi\,\sin\varphi$ as a function of rotation angle φ of the fields relative to the crystal x-axis. Purple represents the pump frequency, blue and red represent the generated signal and idler frequencies, respectively.
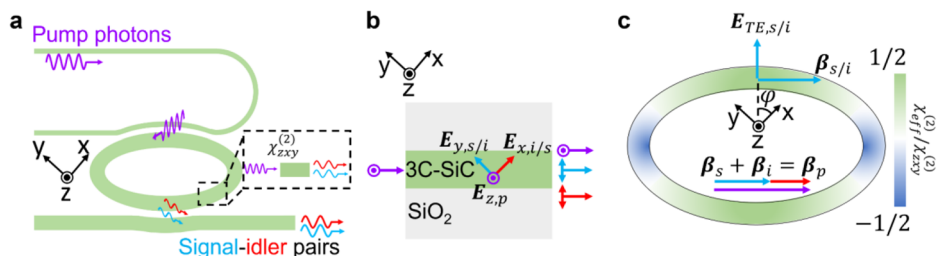
Fig. 2 | Numerical simulations to attain modal phase matching. a Electric-field amplitude distributions of an TE_{00} mode at 1560 nm and of an TM_{20} mode at 780 nm. **b** Effective refractive indices of the pump mode (solid line) and of the signal/idler mode (dashed line) with different 3C-SiC film thicknesses as a function of the waveguide width. **c** Dispersion of the TM_{20} pump mode (solid line) and of the signal/idler TE_{00} mode (dashed line). **d** Calculated map of the non-degenerate difference-frequency generation (DFG) phase-matching condition.
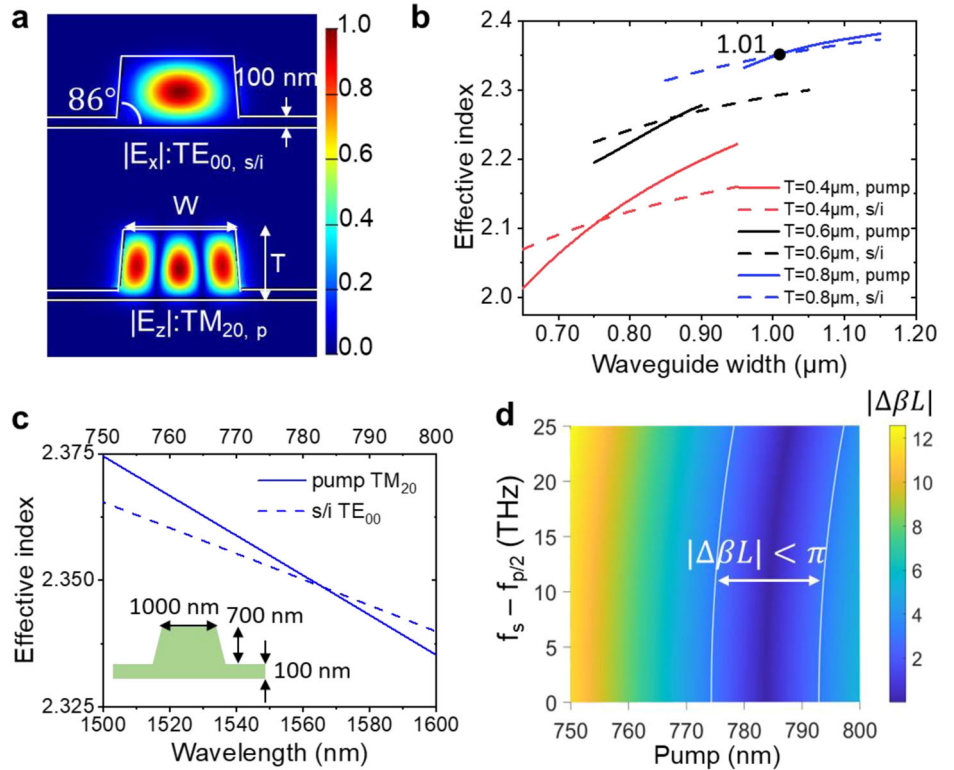
non-degenerate DFG phase-matching condition map with the non-degeneracy $\left(f_s - \frac{f_p}{2}\right)$ between the signal/idler frequencies (satisfying energy conservation) over the pump wavelength, following Fig. 2c. Here, $f_{s(p)}$ is the frequency of the signal (pump) light, respectively. We adopted a total accumulated phase-mismatch of $|\Delta\beta L| = \left|(\beta_p - \beta_s - \beta_i)L\right| < \pi$ within the cavity as a working criterion for defining the MPM region. We notice a pumping wavelength range >10 nm and a non-degeneracy >25 THz. However, a $\pm 50 nm$ of the waveguide width will significantly red- or blue-shift the MPM wavelength window beyond the $1.5 \sim 1.6 \mu m$ wavelengths (see Supplementary Note 2). Finally, we adopted a bus waveguide with the same width of 1000 nm coupled to the microring cavity to input-couple the TE_{00} mode at NIR wavelengths while utilizing a drop waveguide with a narrower width of 400 nm to phase-match the TM_{00} mode in the bus waveguide and in the TM_{20} mode in the microring cavity. The coupling gap spacing is 200 nm for both the coupled waveguides. The interaction length is $15 \mu m$ for the through waveguide and is $30 \mu m$ for the drop waveguide. Both the waveguides are widened to a width of $4 \mu m$ for butt-coupling. Supplementary Note 3 details the device layout and the numerical simulations of the device.

Experimental demonstration of SHG on the 3C-SiCoI chip

We fabricate the device in a cleanroom (see Methods). We characterize the waveguide transmission and SHG from a waveguide-coupled elliptical microring (see experimental details in Supplementary Note 4). The operating device has a designed waveguide of 1050 nm. Given the uncertainty of the actual n_{eff} induced by the continuously varying waveguide curvature within the elliptical cavity and the variance of the waveguide width caused by the fabrication process, we consider this device width a close match to the simulated waveguide width for MPM. Figure 3a shows the scanning electron microscopy (SEM) image of the device. Figure 3b, c shows the SEM images in zoom-in view of the sidewall and in the cross-sectional view of the waveguide end-facet, respectively. We extract a root-mean-square (RMS) of the waveguide sidewall roughness of ~7.3 nm based on analysis of the top-view SEM image (see Supplementary Note 5). This RMS is significantly

larger than the previously reported value on 3C-SiC[16]. Figure 3d shows the near-field image measured at the through waveguide end facet by a charge-coupled device (CCD) camera upon a cavity resonance at 787.7 nm. It shows three intensity maxima, suggesting the cavity resonance has an TM_{20} waveguide mode while the higher-order mode in the through waveguide could be redistributed due to the waveguide tapering. The actual distribution Fig. 3e shows the corresponding lens-to-lens normalized transmission spectra of the device under a stabilized stage temperature of 22 C. The measured transmission spectra in the 780 nm and 1550 nm wavelengths show a good double-resonance alignment for SHG between the resonances of 787.7 nm and 1575.4 nm, as indicated by the zoom-in view of Fig. 3f. The loaded Q factors of the 1575.4 nm and of the 787.7 nm resonances are around 2.5×10^4 and 1.4×10^4, respectively. This is lower than the $Q_{loaded} > 10^5$ we previously reported[11]. By a Lorentzian resonance lineshape fitting, shown as the magenta dashed line in Fig. 3f, we obtain an intrinsic Q factor of ~3.0×10^4 and thereby extract a waveguide loss of ~11 dB cm^{-1} at 1574 nm. The free spectral range (FSR) of the 1575.4 nm and the 787.7 nm resonances are ~6.9 nm (~800 GHz spacing) and ~1.5 nm, respectively. We conduct the waveguide dispersion analysis of the resonance (see Supplementary Note 6).

We fix the pump power of the TE-mode at 1575.4 nm within the through waveguide at ~0.5 mW on-chip power (see Methods) and measure the TM-polarized SHG at the drop waveguide port. Figure 3g shows the corresponding measured SHG spectrum using an optical spectrum analyzer (OSA). The full-width at half-maximum (FWHM) of the pump and of the SHG are limited to the equipment resolution of 0.02 nm. The inset shows the top-view of the SHG scattering signal captured by a CCD camera. As the SHG is a second-order nonlinear harmonic generation driven by simultaneously absorbing two fundamental pump photons, the SHG is signified by a parabolic dependence on the pump power. Figure 3h shows the measured pump-to-SHG power dependence in a log-log scale, revealing a fitted slope of 1.98 ± 0.01 that is consistent with the nature of the SHG. We estimate the on-chip SHG conversion efficiency to be $\eta_{SHG} = \frac{P_{SHG}}{P_p^2} = 17.4 \pm 0.2\% W^{-1}$ with the maximum waveguide end-facet out-coupling loss of 5.8 dB (See Supplementary Note 7 for details). We calculate the theoretical SHG

Fig. 3 | Experimental demonstration of second-harmonic generation on the 3C-SiCoI chip.
Scanning electron microscopy (SEM) images of (**a**) the device, (**b**) the zoom-in view of the sidewall, and of (**c**) the cross-sectional view of the waveguide end-facet. **d** Near-field image of the TM_{20} mode. **e** Corresponding lens-to-lens normalized transmission spectra of the device for 780 nm wavelengths (red) and 1550 nm wavelengths (black). **f** Zoom-in view of the aligned resonances with a Lorentzian resonance lineshape fitting of the NIR resonance. **g** Measured pump (black) and second-harmonic generation (SHG) (red) spectra. Inset: Top-view scattering of the SHG light. **h** Measured and fitted pump-to-SHG power dependence in a log-log scale.
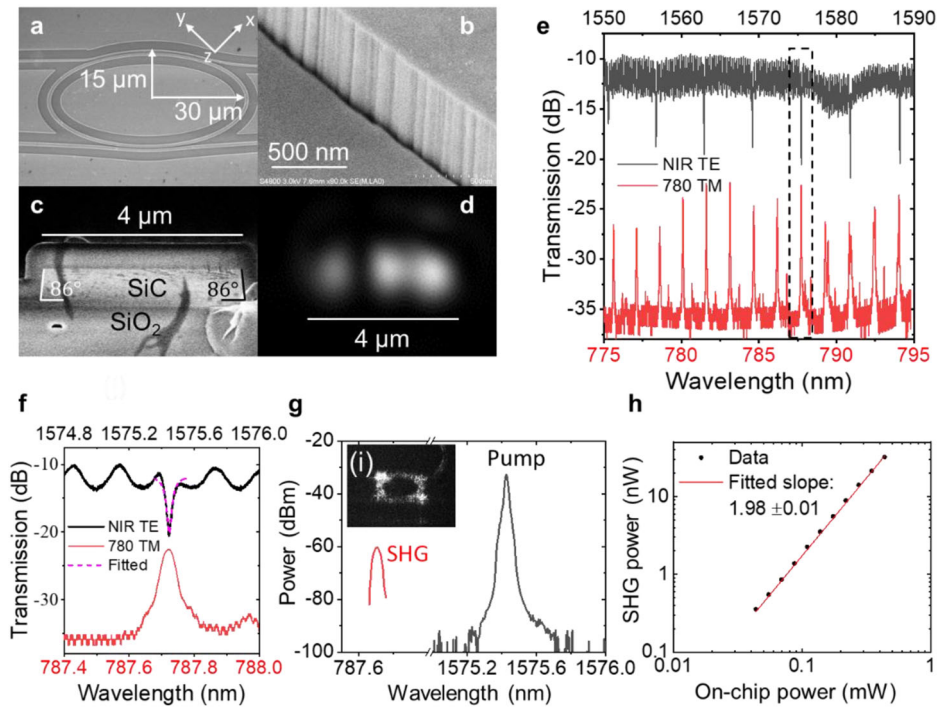
conversion efficiency as follows[37]:

$$\eta_{SHG} = \frac{|\gamma|^2 \omega_2}{\hbar \omega_1^2} \frac{\kappa_{1,e}^2}{\left[\left(\frac{\kappa_{1,t}}{2}\right)^2 + \Delta\omega_1^2\right]^2} \frac{\kappa_{2,e}}{\left(\frac{\kappa_{2,t}}{2}\right)^2 + \Delta\omega_2^2} \qquad (1)$$

where $\omega_{1(2)}$, $\kappa_{1(2),t}$, $\kappa_{1(2),e}$ and $\Delta\omega_{1(2)}$ are the angular frequencies, the cavity total loss rates, the cavity external coupling rates and the angular frequency detuning from the cavity resonances of the 1575 nm pump (SHG) waves. The nonlinear coupling coefficient γ is given by:

$$\gamma = \frac{\omega_1}{4} \sqrt{\frac{2\hbar\omega_2}{\epsilon_0}} \frac{\int \chi^{(2)} E_1 E_1 \cdot E_2^* dV}{\int \epsilon_1 |E_1|^2 dV \sqrt{\int \epsilon_2 |E_2|^2 dV}} \qquad (2)$$

where ϵ_0 is the vacuum permittivity and $\epsilon_{1(2)} = 6.55(6.81)$ is the relative permittivity of 3C-SiC at 1550 nm and 780 nm[11], respectively (See Supplementary Note 8 for details). We estimate a nonlinear coupling of $\gamma \approx 7.6 \times 10^5\,Hz$. From (1), assuming a double-resonance condition, we assume $\Delta\omega_{1(2)} \ll \kappa_{1,t}$. Given our measured loaded-Q factors at 1550 nm and 780 nm and assuming an external coupling $\kappa_{1(2),e} \approx \kappa_{1(2),t}/2$ we theoretically estimated $\eta_{SHG} \approx 19\% W^{-1}$, which is consistent with our experimental estimation.

Table 1 summarizes the state-of-the-art resonance-enhanced SHG results from different SiC platforms[13,19,20]. Our SHG conversion efficiency on 3C-SiCoI is lower than the best value in 4H-SiCoI because of the limited Q factors of our platform at this stage. We characterize the same device for DFG and SPDC processes.

Experimental demonstration of DFG on the 3C-SiCoI chip
We input both the on-resonance near-visible pump and NIR signal waves from the drop- and input-bus waveguides, respectively (see Supplementary Note 4). In each experiment, we fix the pump wavelength λ_p at a cavity resonance around 780 nm and then tune the signal wavelength around different cavity resonances at the blue side of $2\lambda_p$. We fine-tune the pump and signal wavelengths around their respective cavity resonances to maximize the output DFG idler power generated at the red side of $2\lambda_p$ (see

Supplementary Note 9). We fix the estimated on-chip power of pump and signal waves at 4 mW.

Figure 4a–f show the measured spectra using the OSA. The dashed line in each figure denotes the degenerate $2\lambda_p$ positions. The pump cavity resonances supporting triple-resonance DFG span from 786.17 nm to 795.69 nm, giving a pump spectral window of 9.5 nm. We observe cavity-enhanced DFG from at least five different signal cavity resonances. Pumping at a cavity resonance of 795.7 nm, we observe the maximum non-degeneracy of 97 nm. Figure 4g shows in a scatter plot the measured triple-resonance-enhanced DFG modes. However, in comparison with the numerically simulated waveguide dispersion (Fig. 2d), the observed overall spectral range for attaining triple-resonance DFG is narrower. We attribute this to fabrication-induced non-uniformities. While the measured triple-resonance DFG spectral windows are wider than those reported of similar microring cavity-based work on the LNoI[37] and AlN[38] platforms. We also characterize another waveguide-coupled elliptical microring with a designed waveguide width of 1000 nm (see Supplementary Note 10) that shows a blue shift of the overall triple-resonance DFG spectral range, which is consistent with the numerical simulation of the waveguide dispersion (see Supplementary Note 2). Figure 4h shows the measured power-dependence of the DFG. We pump at a 787.7 nm cavity resonance and input a signal at a 1569.2 nm cavity resonance and measure the generated idler power at the corresponding 1581.8 nm cavity resonance. In the log-log scale, the idler power has fitted slopes of 0.96 ± 0.01 and 0.90 ± 0.01 dependence on the pump and on the signal, respectively, as expected from a theoretical linear dependence.

Experimental demonstration of SPDC on the 3C-SiCoI chip
We describe the experimental setup in Supplementary Note 4. We fix the pump wavelength λ_p at a cavity resonance at 787.7 nm and measure the SPDC with two-channel superconducting nanowire single-photon detectors (SNSPDs). The SNSPDs feature dark counts of ~100 Hz for each of the two channels. Figure 5a shows the measured single-photon flux detected by the SNSPDs with different dense wavelength-division multiplexed (DWDM) channels that span the corresponding cavity resonance wavelengths in the NIR. The estimated on-chip pump power is 5.8 mW, which is the maximum on-chip power obtainable from our setup using a

continuous-wave semiconductor laser. We register the photon arrival times from two non-degenerate photon-pairs, namely 1569/1581 nm and 1563/1588 nm, by the time-digit converter (TDC) with a resolution of 5 ps per bin. Figure 5b, c shows the measured histograms of the relative arrival times of the two pairs of channels at a pump power of 5 mW, which feature strong coincidence. We record 60 s of data for each pair for statistics. We adopted a double-side exponential decay relation $N_{si}(t) = N_0 e^{-|t|/\tau}$ to fit the data,

Table 1 | Summary of resonance-enhanced SHG results from SiC platforms

Platform	Structure	Phase-matching	Q factor (10^4)	η_{SHG} (% W^{-1})
4H-SiCoI[19]	Microring	MPM	8 @1555 nm 2 @777.5 nm	360
4H-SiC[20]	Suspended disk	–	710 @1554.2 nm	3.91
6H-SiCoI[13]	Photonic crystal	–	1 @1560 nm	15[a]
3C-SiCoI (This work)	Microring	MPM	2.5 @1575.4 nm 1.4 @787.7 nm	17.4

[a]The experiment adopts a pulsed laser. This value is calculated based on average powers.

where $N_{si}(t)$, N_0 and τ are the coincidence count in the time-bin at delay t, the maximum coincidence count at zero-time delay and the photon life-time. The fitted value of $\tau = 26 \pm 1$ps for both the pairs correspond to the loaded Q factor of $\sim 2.5 \times 10^4$ in the NIR wavelengths, which is consistent with our transmission resonance measurements (see Fig. 3e). We define the coincidence counts summed up from the 12 bins within the $\pm \tau$ range of the histograms as the total coincidence count N_{si}.

For the SPDC, which is a spontaneous second-order nonlinear generation of photon pairs by down-converting one pump photon, the SPDC is signified by a linear dependence on the pump power. Figure 5d, e shows the measured power-dependence of the single-channel counts and of the photon-pair coincidence counts. We estimate the PGR inside the cavity by $PGR = \frac{N_s N_i}{N_{si}}$, where $N_{s(i)}$ are the single-channel counts from the signal (idler) flux. Figure 5f shows the estimated PGR. We observe a good linearity of the estimated PGR and obtain by linear fitting a pair generation efficiency of 0.94 ± 0.02 MHz mW^{-1} (1569–1581 nm) and 1.32 ± 0.07 MHz mW^{-1} (1562–1588 nm). We calculate the theoretical PGR assuming the triple-resonance condition as follows[38]:

$$PGR = \frac{32\gamma^2}{\kappa_{i,t} + \kappa_{s,t}} \frac{\kappa_{p,e}}{\kappa_{p,t}^2} \frac{P_p}{\hbar\omega_p} \qquad (3)$$
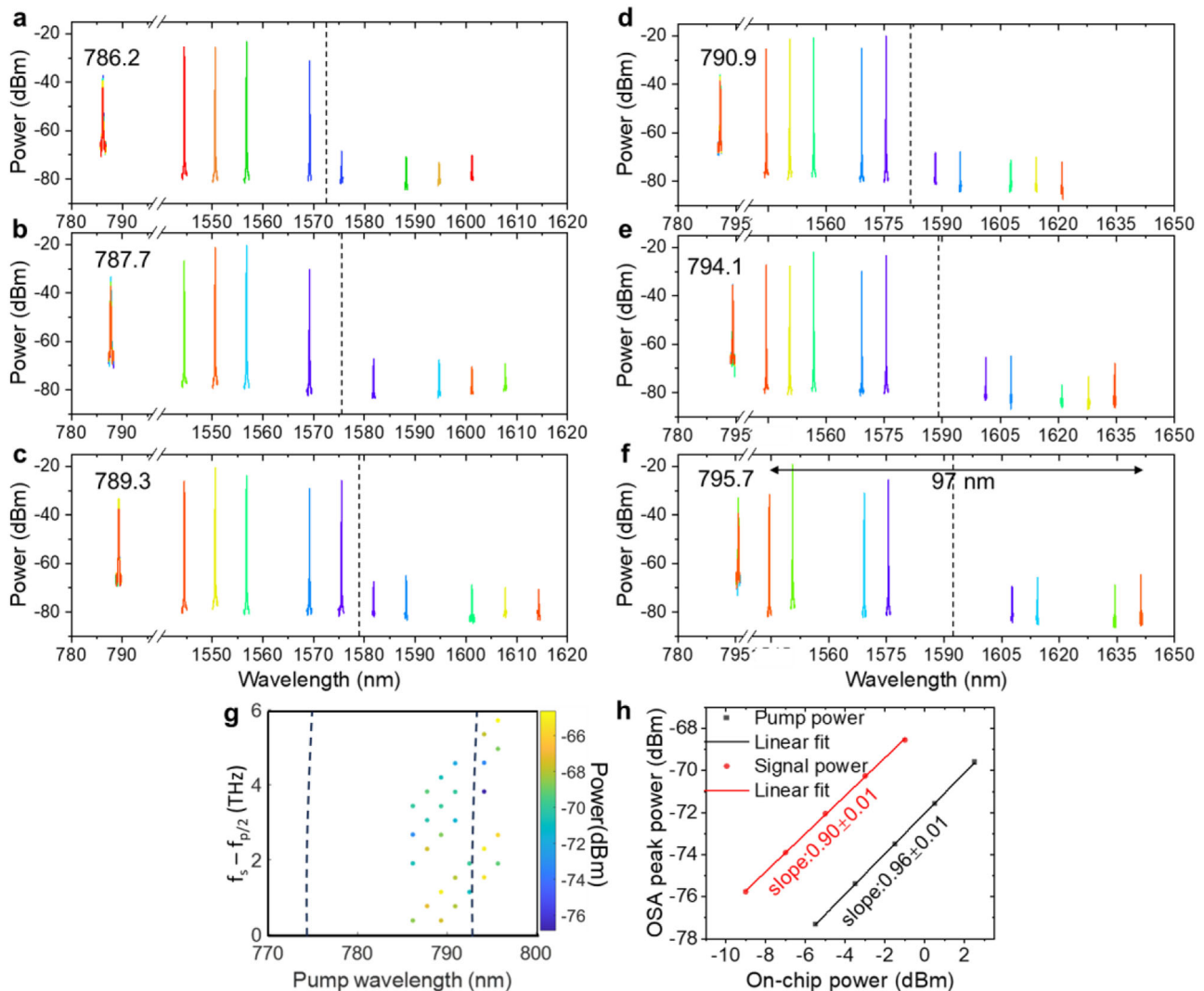

Fig. 4 | Experimental demonstration of difference-frequency generation on the 3C-SiCoI chip. a–f Measured difference-frequency generation (DFG) spectra with different input pump and signal resonances. Different colors represent various groups of pump, signal and generated idler wavelengths. **g** Scatter plot of the triple-resonance-enhanced DFG modes. The region between the two dashed lines corresponds to the simulated MPM zone in Fig. 2d. **h** Measured power-dependence of the DFG with varying pump and observed signal powers.

Fig. 5 | Experimental demonstration of spontaneous parametric down conversion on the 3C-SiCoI chip. a Measured single-photon flux detected by the SNSPDs with different DWDM channels. SNSPDs: superconducting nanowire single-photon detectors. DWDM channels: dense wavelength-division multiplexed channels. FSR: free spectral range. **b**, **c** Measured histograms of the relative arrival times of the first adjacent resonances at 1569/1581 nm and of the second adjacent resonances at 1563/1588 nm, respectively. The histograms are measured multiple times to obtain the error bars for all the bins. Measured power dependence of: (**d**) the single-channel counts, (**e**) the photon-pair coincidence counts, (**f**) the estimated PGRs, and of (**g**) the estimated CARs. The error bars are the standard deviations of (**b**–**e**) the coincidence counts, (**f**) PGRs and of (**g**) CARs.
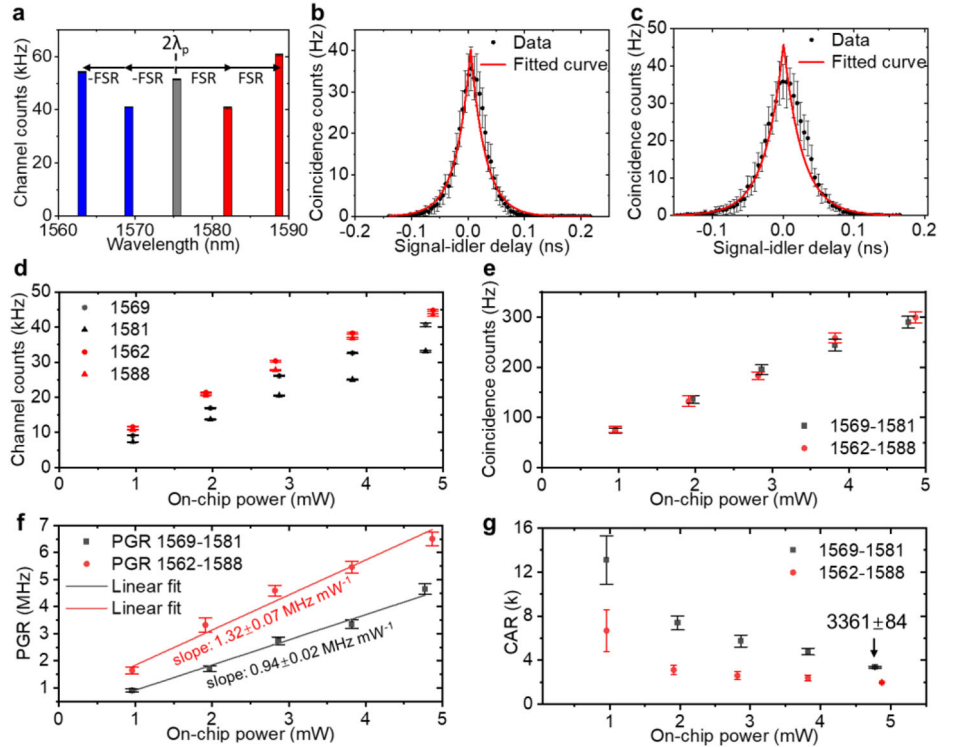
Assuming $\kappa_{p,e} \approx \kappa_{p,t}/2$, we obtain from Eq. (3) the theoretical PGR efficiency of $\frac{PGR}{P_p} = 2.3\,\mathrm{MHzmW^{-1}}$, which is close to our measured result. Our estimated PGR values are smaller than those reported values of the AlN platform[38] and of the LNoI platform[39]. We attribute this to our un-optimized device fabrication process, as the pair-generation efficiency is primarily determined by the total cavity loss (see Eq. (3)). Figure 5g shows the CAR of the two pairs, given by $CAR = \frac{N_{si}}{N_{\mathrm{noise}}}$. Here we integrate the rare coincidence counts 1 ns away from the central peak of the coincidence counts to obtain an average coincidence count per bin and multiply the 12 number of bins adopted in the summation of N_{si} to obtain the N_{noise} (see Supplementary Note 11). We obtain a high $CAR = 3361 \pm 84$ upon pumping at the on-chip power of 5 mW from the 1569/1581 nm photon-pairs. We also characterize the SPDC process using another device with a designed waveguide width of 1000 nm (see Supplementary Note 12). As indicated by the DFG process, this device generates photon-pairs in the C-band channels.

Experimental demonstration of heralded single-photon sources
We describe the experimental setup in Supplementary Note 4. By adopting the firing of the idler channel as the gating, we measure the signal channel as a heralded single-photon source. We utilize a fiber-based 50:50 beam splitter in the signal path to test the single-photon nature. The heralded second-order coherence is characterized by[40]:

$$g_H^{(2)} = \frac{N_{s_1 s_2 i} N_i}{N_{s_1 i} N_{s_2 i}} \qquad (4)$$

where $N_{s_1 s_2 i}$ is the triple-coincidence counts for both the beam-split signal channels and the heralding idler channel and $N_{s_{1(2)}i}$ are the coincidence counts between the one split signal channel and the heralding idler channel. Equation (4) indicates that the noise from the idler (heralding) channel has a dominant effect. To reduce the influence, we assign one channel of the low-noise SNSPD for heralding, while using another SNSPD channel and one extra avalanche photodetector for detecting signals 1 and 2, respectively.

We accumulate more than 6 h of data (40 Gb) and obtain only 1 triple coincidence count $N_{s_1 s_2 i}$ while collecting $N_{s_1 i} = 1{,}949{,}638$, $N_{s_2 i} =$ 441, 670 and $N_i = 610, 078, 920$. Assuming a Poissonian distribution[40] of the triple coincidence event, we estimate a low $g_H^{(2)} = 0.0007$ and a confidence interval of (0.0001, 0.002) within approximately one standard deviation. This is one order of magnitude below recently reported work using second- and third-order SPDC processes[38–41]. Hence, our device can function as low-noise heralded single-photon sources.

Table 2 summarizes the state-of-the-art microring-based quantum light sources from different second-order nonlinear platforms[38,39]. Although our PGR is limited by our Q factors, we have demonstrated a low-noise performance with the lowest $g_H^{(2)}$ among all the platforms.

Experimental demonstration of time-bin entanglement
To demonstrate the potential of building a quantum system based on our 3C-SiCoI platform, we examine time-bin entanglement using our photon-pair sources. Entangled photon-pairs constitute many quantum-enabled technologies, including quantum computing and quantum cryptography[42]. Among various physical dimensions for entanglement, time-bin entanglement is more robust to perturbations when the photons propagate in fiber networks[42–45].

Figure 6a illustrates the principle of generating time-bin entanglement using a free-space Franson unbalanced interferometer. The photon-pairs can simultaneously travel through the short arm together and the long arm together, which are indistinguishable. The photon-pairs can also travel through the short arm and the long arm separately, which are distinguishable. When the photons re-enter the fiber system and routed to SNSPDs through the DWDM filters, the recorded histogram of their relative arrival times is shown in the Inset. We attribute the two side peaks as the distinguishable events that the two photons propagate in different arms. The central time-bin measures the photon-pair in an entangled state as $|\psi> = \frac{1}{\sqrt{2}}(|SS>_{si} + e^{i(\varphi_s + \varphi_i)}|LL>_{si})$, where S(L) and $\varphi_s(\varphi_i)$ denote the short (long) arm and the optical phase difference between the two arms of the signal (idler) photon. To separate the central peak time-bin from the side peak time-bins, we unbalance the interferometer arms by exceeding the coherence length of the photons limited by the cavity lifetime, calculated by $L_c = \tau c$, which is 7.8 mm for our case.

Table 2 | Summary of microring-based quantum light sources from various platforms

Platform	Q_p ($\times 10^4$)	$Q_{s/i}$ ($\times 10^4$)	Pump power (mW)	PGR (MHz)	CAR	$g_H^{(2)}$
AlNoI[38]	11	20	1.9	11	–	0.088
LNoI[39]	15	10	0.0034	2.5	451	0.008
3C-SiCoI (This work)	2.5	1.4	5	4.8	3361	0.0007

We insert the free-space interferometer into the down-stream of the SPDC experimental setup to prepare the entanglement. We pump at 787.7 nm with an estimated 5 mW on-chip power and measure the photon-pair channels of 1569/1581 nm. Figure 6b shows the measured histograms at two different piezo-voltage settings fine-tuning the interferometer long arm. The three-peak time-bins are separated by a time difference of 0.58 ns, corresponding to a path difference of 17.4 cm. The coincidence counts at the $|SS>_{si}$ and $|LS>_{si}$ time-bins are not sensitive to the piezo-voltage while the total coincidence counts in the central time-bin vary sinusoidally with the piezo-voltage. The quantum interference between the superposed photon-pair states $|SS>_{si}$ and $|LL>_{si}$ yields a sinusoidal modulation of the coincidence counts (assuming 50:50 beam splitters) as $0.5N_{max}[1 + V\cos(\varphi_s + \varphi_i)]$, where N_{max} and V are the maximum transmitted central time-bin counts and the visibility of the quantum interference. Figure 6c, d shows the measured channel counts of the signal/idler photons and the measured coincidence counts of the central time-bin, respectively. Each data point corresponds to a data collection spanning 30 s. We do not observe first-order (single-photon) quantum interference as the interferometer path difference is significantly longer than the photon cavity coherence time so the two wave-packets of the same photon simultaneously traveling in the two different interferometer arms cannot meet each other. We observe second-order quantum interference in the coincidence counts in the central time-bin. Using a sinusoidal fitting, we extract a visibility of $V = 86.0 \pm 2.4\%$. This is significantly exceeding the Bell's inequality limit of 70.1%[23], indicating a clear time-bin entanglement. We attribute the non-ideal visibility to the drifts of the optical alignment and collimation conditions of the two interferometer arms during the experiment. We note that our Franson interferometer is not actively stabilized, and thus phase drift is

potentially the main source of fringe visibility degradation. In our future work, we could employ active stabilization on the interferometer to overcome the issue. We note that the superposed $|SS>_{si}$ and $|LL>_{si}$ states do not have the same probability amplitudes in practice due to different setup insertion losses for the two interferometer arms.

Conclusion

We demonstrated experimentally that our integrated 3C-SiCoI photonic platforms enable nonlinear and quantum light sources using waveguide-coupled elliptical microring cavities. We realized quantum interference systems, namely, time-bin entanglement using our photon-pair sources. By exploiting a wafer-scale bonding process, we envision the feasibility to fabricate on a chip large-scale-integrated cavities and on-chip interferometers. Our work thus paves the way toward future large-scale-integrated on-chip nonlinear and quantum photonic circuits based on this CMOS-compatible second-order nonlinear photonic platform. Besides, the recently demonstrated Pockels-effect-based 3C-SiC optical modulator[21] can be integrated on the same quantum photonic chip to provide even more complex quantum state manipulation functionalities. Our measured SHG conversion and pair-generation generation efficiencies are, however, still below those state-of-the-art values from other on-chip second-order nonlinear photonic platforms, including LNoI[38], GaAs[36] and 4H-SiC[19]. The work reported in those platforms are based on resonators supporting loaded Q factors of $10^5 \sim 10^6$. We attribute our limited $Q \sim 10^4$ to our un-optimized fabrication process, where the waveguide sidewall roughness resulting from the dry etching causes significant scattering losses. Given our near-vertical waveguide sidewall slope of 86°, we can fabricate thicker 3C-SiC devices with a wider waveguide width, which can increase the waveguide confinement and reduce the sidewall scattering loss. The scattering losses caused by the crystal lattice defects within the 3C-SiC film can limit the cavity Q factor as well. Those defects are generated during the epitaxial process because of the large (20%) lattice mismatch between the 3C-SiC and the Si substrates. We can mitigate this issue by adopting thicker epitaxial layers, which relax the crystal lattice defects due to the lattice mismatch gradually with the film thickness[46–48], and by thinning down the films to the target thickness while removing the high-density crystal defects near the interface with the Si substrate."

Finally, there are rooms for our elliptical microring to further enhance the cavity-roundtrip nonlinear interaction coefficient γ. For example, the ellipse of a larger a/b aspect ratio can further align the cavity along the

Fig. 6 | Preparation of the time-bin entanglement using the 3C-SiCoI photon-pair source.
a Illustration of the principle of generating time-bin entanglement using a free-space Franson unbalanced interferometer. Inset (i): Illustration of the three-time-bin histogram. **b** Measured histograms at two different piezo-voltage settings. **c** Measured single-channel counts with different piezo-voltage settings. **d** Measured coincidence counts of the central bin upon various piezo-voltage settings and fitted with a sinusoidal function.
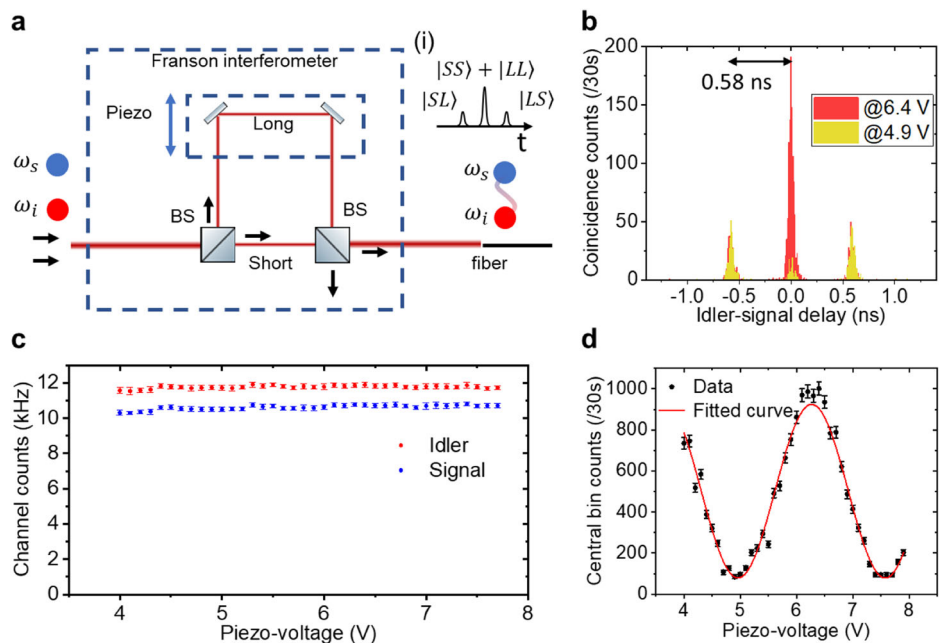
orientation that enables the maximum $\chi_{eff}^{(2)}$ (see Supplementary Note 13). However, the design tradeoff is reducing the bending radius of the high-curvature poles by the relation $R_{pole} = \frac{b^2}{a}$. To provide further elongation while avoiding a larger bending curvature, other non-circular microring configurations can also be explored, including racetracks with Euler bending[49] and Bezier bending[50] designs. However, special optimization of these bending structures may be required to reduce the straight-to-curve transition loss of the two different modes at the pump/signal wavelengths simultaneously. Nonlinear and quantum light sources based on the 4-bar QPM are possible due to the point-group symmetry of 3C-SiC.

Methods
Device fabrication
We fabricate the devices on the same integrated 3C-SiCoI platform as described in[9]. We use the commercially available polished 4" (001) 3C-SiC-on-Si wafers from NOVASIC. Before the wafer bonding, we deposit a layer of plasma-enhanced chemical vapor deposition (PECVD) SiO_2 with a thickness of 500 nm on the 3C-SiC-on-Si dies (1×1 cm) to serve as a high-quality under-cladding layer. The PECVD recipe features SiH_4 and N_2O gas flows of 15 and 1410 sccm, respectively. The chamber is heated to 300 °C and kept at a pressure of 900 mTorr. The coil power is 30 W. We use the Karl Suss SB6 wafer bonder for the anodic bonding process between the dies and the soda lime glass substrate. We attain the bonding under 380 °C in a vacuum environment and upon an applied voltage of 1000 V. We use the standard 25% tetramethylazanium hydroxide solution to completely remove the silicon substrate at 80 °C and to expose the 3C-SiC film. The thickness of the 3C-SiC film is 1.5 μm initially. We thin down the film to our targeted thickness of ~800 nm by deep reactive ion etching (DRIE) process. The etching chemistry adopts SF_6 and O_2 gases with flows of 25 and 5 sccm, respectively. We kept the chamber pressure at 10 mTorr. The coil power and the platen power are 800 and 250 W, respectively. We then deposit a layer of the PECVD SiO_2 as the hard mask. We pattern it with electron-beam lithography and with a standard SiO_2 dry etching process available in the cleanroom. This SiO_2 hardmask etching recipe adopts C_4F_8 and H_2 gases with gas flows of 12 and 8 sccm, respectively. We kept the chamber pressure at 4 mTorr. The coil power and the platen power are 925 and 130 W, respectively. Then, we use the same SF_6-based etching chemistry as in the film thinning-down process to dry etch the 3C-SiC patterns. To attain a steep sidewall slope, we add 3 s of C_4F_8 passivation steps after 5 s of dry etching steps to protect the waveguide sidewalls. The gas flow of C_4F_8 is 40 sccm and the coil power is 200 W. We recorded an etching selectivity of 3C-SiC:$SiO_2 \approx 1.45$. Afterwards, we deposit a layer of PECVD SiO_2 with a thickness of 500 nm as the upper-cladding layer. Finally, we cleave the chip to expose the waveguide end-facets for coupling using long-working-distance (LWD) objective lenses.

Estimation of the on-chip power
We estimate the on-chip power based on the power measured by an OSA considering the insertion losses of the lens-to-fiber coupling, the OSA and of the waveguide output end-facets. The measured insertion losses of the lens-to-fiber coupling and of the OSA are 3.0 dB and 2.4 dB, respectively. We then estimated the output power. The insertion loss of a test straight waveguide fabricated adjacent to the device is slightly below 12.0 dB for both the 780 nm and 1550 nm wavelengths. We neglect the waveguide propagation loss over this 1.2 mm long waveguide and adopted an average waveguide end-facet out-coupling loss as 5.8 dB as the maximum out-coupling loss, assuming the waveguide end-facet in-coupling loss is equal to or larger than the out-coupling loss, for estimating the on-chip power for both the 780 nm and 1550 nm light.

Data availability
All the data employed for this work will be made available from the authors upon reasonable request.

References
1. She, X., Huang, A. Q., Lucia, O. & Ozpineci, B. Review of Silicon Carbide Power Devices and Their Applications. *IEEE Trans. Ind. Electron.* **64**, 8193–8205 (2017).
2. Bogdanov, S., Shalaginov, M. Y., Boltasseva, A. & Shalaev, V. M. Material platforms for integrated quantum photonics. *Opt. Mater. Express* **7**, 111 (2017).
3. Lu, X., Lee, J. Y. & Lin, Q. High-frequency and high-quality silicon carbide optomechanical microresonators. *Sci. Rep.* **5**, 1–9 (2015).
4. Yamaoka, S. et al. Directly modulated membrane lasers with 108 GHz bandwidth on a high-thermal-conductivity silicon carbide substrate. *Nat. Photonics* **15**, 28–35 (2021).
5. Wang, J. et al. Bright room temperature single photon source at telecom range in cubic silicon carbide. *Nat. Commun.* **9**, 4106 (2018).
6. Radulaski, M. et al. Scalable Quantum Photonics with Single Color Centers in Silicon Carbide. *Nano Lett.* **17**, 1782–1786 (2017).
7. Wu, I. J. & Guo, G. Y. Second-harmonic generation and linear electro-optical coefficients of SiC polytypes and nanotubes. *Phys. Rev. B Condens. Matter Mater. Phys.* **78**, 1–10 (2008).
8. Sato, H., Shoji, I., Suda, J. & Kondo, T. Accurate measurements of second-order nonlinear-optical coefficients of silicon carbide. *Mater. Sci. Forum* **615 617**, 315–318 (2009).
9. Romijn, J. et al. Integrated Digital and Analog Circuit Blocks in a Scalable Silicon Carbide CMOS Technology. *IEEE Trans. Electron Devices* **69**, 4–10 (2022).
10. Xu, Y. et al. Mitigating photorefractive effect in thin-film lithium niobate microring resonators. *Opt. Express* **29**, 5497 (2021).
11. Li, J. & Poon, A. W. A 3C-SiC-on-Insulator-Based Integrated Photonic Platform Using an Anodic Bonding Process with Glass Substrates. *Micromachines* **14**, 399 (2023).
12. Powell, K. et al. High-Q suspended optical resonators in 3C silicon carbide obtained by thermal annealing. *Opt. Express* **28**, 4938 (2020).
13. Yamada, S. et al. Second-harmonic generation in a silicon-carbide-based photonic crystal nanocavity. *Opt. Lett.* **39**, 1768 (2014).
14. Martini, F. & Politi, A. Four wave mixing in 3C SiC ring resonators. *Appl. Phys. Lett.* **112**, 1–5 (2018).
15. Lu, X., Lee, J. Y., Rogers, S. & Lin, Q. Optical Kerr nonlinearity in a high-Q silicon carbide microresonator. *Opt. Express* **22**, 30826 (2014).
16. Fan, T., Moradinejad, H., Wu, X., Eftekhar, A. A. & Adibi, A. High-Q integrated photonic microresonators on 3C-SiC-on-insulator (SiCOI) platform. *Opt. Express* **26**, 25814 (2018).
17. Guidry, M. A. et al. Optical parametric oscillation in silicon carbide nanophotonics. *Optica* **7**, 1139 (2020).
18. Guidry, M. A., Lukin, D. M., Yang, K. Y., Trivedi, R. & Vučković, J. Quantum optics of soliton microcombs. *Nat. Photonics* **16**, 52–58 (2022).
19. Lukin, D. M. et al. 4H-silicon-carbide-on-insulator for integrated quantum and nonlinear photonics. *Nat. Photonics* **14**, 330–334 (2020).
20. Wang, C. et al. High-Q microresonators on 4H-silicon-carbide-on-insulator platform for nonlinear photonics. *Light Sci. Appl.* **10**, 139 (2021).
21. Powell, K. et al. Integrated silicon carbide electro-optic modulator. *Nat. Commun.* **13**, 1–7 (2022).
22. Wang, R., Li, J., Cai, L. & Li, Q. "Investigation of the electro-optic effect in high-Q 4H-SiC microresonators,". *Opt. Lett.* **48**, 1482–1485 (2023).
23. Franson, J. D. Bell inequality for position and time. *Phys. Rev. Lett.* **62**, 2205–2208 (1989).
24. Li, J. & Poon, A. W. Time-bin Entanglement Based on Integrated 3C-SiC-on-insulator Photon-pair Sources. In *Proceedings of CLEO* (San Jose, USA, 2023).

25. Jerphagnon, J. & Kurtz, S. K. Maker fringes: A detailed comparison of theory and experiment for isotropic and uniaxial crystals. *J. Appl. Phys.* **41**, 1667–1681 (1970).

26. Niedermeier, S., Schillinger, H., Sauerbrey, R., Adolph, B. & Bechstedt, F. Second-harmonic generation in silicon carbide polytypes. *Appl. Phys. Lett.* **75**, 618–620 (1999).

27. Lundquist, P. M., Lin, W. P., Wong, G. K., Razeghi, M. & Ketterson, J. B. Second harmonic generation in hexagonal silicon carbide. *Appl. Phys. Lett.* **66**, 1883–1885 (1995).

28. Fiorentino, M. et al. Spontaneous parametric down-conversion in periodically poled KTP waveguides and bulk crystals. *Opt. Express* **15**, 7479–7488 (2007).

29. Kaneda, F., Suzuki, H., Shimizu, R. & Edamatsu, K. Direct generation of frequency-bin entangled photons via two-period quasi-phase-matched parametric down conversion. *Opt. Express* **27**, 1416 (2019).

30. Dong, N., Chen, F. & Vázquez de Aldana, J. R. Efficient second harmonic generation by birefringent phase matching in femtosecond-laser-inscribed KTP cladding waveguides. *Phys. Status Solidi Rapid Res. Lett.* **6**, 306–308 (2012).

31. Lin, J. et al. Phase-Matched Second-Harmonic Generation in an On-Chip $LiNbO_3$ Microresonator. *Phys. Rev. Appl.* **6**, 1–6 (2016).

32. Harris, G. L. *Properties of silicon carbide* (Institution of Electrical Engineers, London, 1995).

33. Orais, N. M. et al. Directionally induced quasi-phase matching in homogeneous AlGaAs waveguides. *Opt. Lett.* **42**, 4287–4290 (2017).

34. Kuo, P. S., Bravo-Abad, J. & Solomon, G. S. Second-harmonic generation using 4-quasi-phasematching in a GaAs whispering-gallery-mode microcavity. *Nat. Commun.* **5**, 1–7 (2014).

35. Mariani, S. et al. Second-harmonic generation in AlGaAs microdisks in the telecom range. *Opt. Lett.* **39**, 3062–3065 (2014).

36. Chang, L. et al. Strong frequency conversion in heterogeneously integrated GaAs resonators. *APL Photonics* **4**, 036103 (2019).

37. Luo, R. et al. Optical Parametric Generation in a Lithium Niobate Microring with Modal Phase Matching. *Phys. Rev. Appl.* **11**, 1 (2019).

38. Guo, X. et al. Parametric down-conversion photon-pair source on a nanophotonic chip. *Light Sci. Appl.* **6**, 1–8 (2017).

39. Ma, Z. et al. Ultrabright Quantum Photon Sources on Chip. *Phys. Rev. Lett.* **125**, 263602 (2020).

40. Wu, K., Zhang, Q. & Poon, A. W. Integrated Si_3N_4 microresonator-based quantum light sources with high brightness using a subtractive wafer-scale platform. *Opt. Express* **29**, 24750 (2021).

41. Ma, C. et al. Silicon photonic entangled photon-pair and heralded single photon generation with CAR > 12,000 and g(2)(0) < 0.006. *Opt. Express* **25**, 32995 (2017).

42. Kwon, O., Park, K.-K., Ra, Y.-S., Kim, Y.-S. & Kim, Y.-H. Time-bin entangled photon pairs from spontaneous parametric down-conversion pumped by a cw multi-mode diode laser. *Opt. Express* **21**, 25492 (2013).

43. Sheng, Y. B. & Zhou, L. Deterministic polarization entanglement purification using time-bin entanglement. *Laser Phys. Lett.* **11**, 085203 (2014).

44. Xue, G. T. et al. Ultrabright Multiplexed Energy-Time-Entangled Photon Generation from Lithium Niobate on Insulator Chip. *Phys. Rev. Appl.* **15**, 1 (2021).

45. Brendel, J., Gisin, N., Tittel, W. & Zbinden, H. Pulsed Energy-Time Entangled Twin-Photon Source for Quantum Communication. *Phys. Rev. Lett.* **82**, 2594–2597 (1999).

46. Wang, L. et al. Growth of 3C-SiC on 150-mm Si (100) substrates by alternating supply epitaxy at 1000 °C. *Thin Solid Films* **519**, 6443–6446 (2011).

47. Severino, A. 3C-SiC epitaxial growth on large area silicon: Thin films. *Silicon Carbide Epitaxy* **37**, 145–191 (2012).

48. Zielinski, M. et al. Structural Quality, Polishing and Thermal Stability of 3C-SiC/Si Templates. *Mater. Sci. Forum* **924**, 306–309 (2018).

49. Jiang, X., Wu, H. & Dai, D. Low-loss and low-crosstalk multimode waveguide bend on silicon. *Opt. Express* **26**, 17680 (2018).

50. Dorin, B. & Ye, W. Two-mode division multiplexing in a silicon-on-insulator ring resonator. *Opt. Express* **22**, 4547–4558 (2014).

Acknowledgements

Author contributions

Jiayang Li designed, simulated, fabricated and characterized the devices. Qianni Zhang and Jiantao Wang performed the characterization of the pump-to-SHG power dependence and the data analysis of SHG. Jiayang Li, Qianni Zhang, Jiantao Wang and Andrew W. Poon wrote the manuscript. Andrew W. Poon supervised this project.

Competing interests

The authors declare no competing interests.

Additional information

Supplementary information The online version contains supplementary material available at https://doi.org/10.1038/s42005-024-01620-x.

Correspondence and requests for materials should be addressed to Andrew W. Poon.

Peer review information *Communications Physics* thanks Florian Kaiser and the other anonymous, reviewer(s) for their contribution to the peer review of this work.

Reprints and permissions information is available at http://www.nature.com/reprints

Publisher's note Springer Nature remains neutral with regard to jurisdictional claims in published maps and institutional affiliations.